ACS Sustainable Chemistry & Engineering

pubs.acs.org/journal/ascecg

Research Article

Effects of Biochar as a Green Additive on the Self-Healing and Properties of Sustainable Cementitious Materials

Babak Vafaei and Ali Ghahremaninezhad*

Cite This: *ACS Sustainable Chem. Eng.* 2024, 12, 8261−8275

Read Online

ACCESS | Metrics & More | Article Recommendations

ABSTRACT: The self-healing, fresh properties, hydration, and other characteristics of the cement paste modified with biochar as a green additive were explored in this work. Evaluation of early-age hydration was conducted using setting time measurement and isothermal calorimetry, and later-age hydration was investigated using thermogravimetric analysis. The mechanical and transport properties were investigated by using compressive strength and electrical resistivity measurements, respectively. The chemical characterization of the healing products was conducted via Fourier transform infrared spectroscopy, scanning electron microscopy equipped with X-ray energy-dispersive spectroscopy, and thermogravimetric analysis. The mechanical strength recovery and crack filling were examined using the three-point bend test and optical microscopy, respectively. The paste with biochar showed an increased setting time and delayed hydration at an early age because of reduced alkali concentrations in the pore solution due to alkali uptake by biochar. However, at later ages, the hydration was improved in the paste with biochar, which is attributed to internal curing. Biochar effectively decreased autogenous shrinkage in the paste, which is attributed to internal curing. Biochar was shown to reduce the electrical resistivity and compressive strength of the cement paste due to higher overall water/cement and macrovoid formation, respectively. The chemical characterization of the healing products showed that they are primarily made up of calcium−silicate−hydrate, calcium carbonate, calcium hydroxide, and ettringite. The content of calcium carbonate was increased in the healing products of the paste with biochar relative to the control paste. The mechanical strength recovery and crack filling were improved in the paste with biochar relative to the control paste, indicating the positive impact of biochar on the self-healing of the paste.

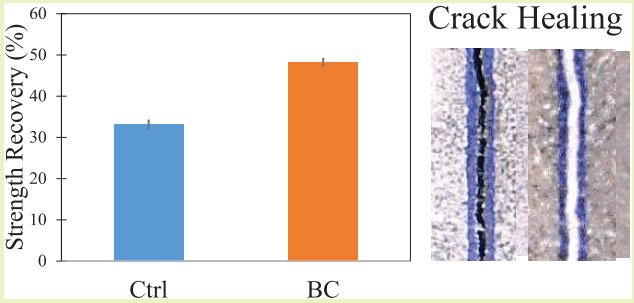

KEYWORDS: *biochar, self-healing, healing products, cement paste*

1. INTRODUCTION

High CO_2 emission is a major concern regarding Portland cement production, and it has spurred efforts to develop solutions to lower the carbon footprint of Portland cement in infrastructure.[1,2] Utilizing alternative materials derived from biowaste to decrease cement demand is one of the effective ways to lower the carbon footprint and enhance the sustainability of construction materials. Biochar is one such material that is obtained via the pyrolysis of biowaste.[3] During processing, carbon present in the biowaste is sequestered in the molecular structure of biochar; the utilization of biochar in construction materials prevents the release of this carbon into the atmosphere via the decay or degradation of biowaste.[3] The carbon sequestration property of biochar in construction materials has been recognized and investigated in detail in the past investigations.[4−6] In addition, the utilization of biochar in the infrastructure sector can be an effective way to reduce the amount of landfilled biowaste. Because of its water absorption and retention capability, biochar has been applied to cement-based materials to enhance their strength and permeability due to the internal curing effect.[7] In another study, the use of biochar at the addition rate of 0.8−1% was shown to increase the modulus of rupture and fracture energy of cementitious materials, which was[8] attributed to the tortuosity of the crack path.[8]

It is now well understood that cementitious materials are prone to crack formation as a result of mechanical and environmental stressors. Microcracks facilitate the entry of external chemical agents into the cementitious material that results in continued damage and loss of mechanical capacity in structures.[9] Thus, structures made of cementitious materials need continued repair and maintenance that are expensive and increase the environmental impacts associated with the

Received: March 8, 2024
Revised: April 30, 2024
Accepted: May 1, 2024
Published: May 10, 2024

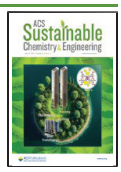

https://doi.org/10.1021/acssuschemeng.4c02045
ACS Sustainable Chem. Eng. 2024, 12, 8261−8275

construction industry.[10] The manual repair that typically involves spraying or injection of chemical sealants has many limitations, including low thermal resistivity, material incompatibility, volume change, delamination, and human hazards.[11]

Thus, over the past decades, self-healing cementitious materials have received significant attention.[12−18] Cementitious materials have an intrinsic ability for self-healing through continued hydration of unreacted cement particles on the crack surface, pozzolanic activity, and calcium carbonate precipitation.[19−24] The presence of water is key to the intrinsic self-healing capability of cementitious materials; however, water is not always accessible in the crack for the self-healing reactions to occur. The use of agents, such as hydrogels, with the ability to absorb and retain water from the environment and release that for the above reactions, can be an effective means to enhance the self-healing properties of cementitious materials.[15,19,25−30] Similar to hydrogels, biochar can absorb and retain water and, as such, can improve the self-healing properties of cementitious materials. However, the effect of biochar on the self-healing of cementitious materials has not been investigated in the past and is not well understood. It should be noted that there have been a couple of prior studies that examined biochar as an immobilizing medium of bacteria for self-healing applications;[10,31] however, the role of biochar alone on the self-healing has not received attention in the past. In addition, there have been only a limited number of prior works that focused on the internal curing and autogenous shrinkage of cementitious materials modified with biochar.[3,32−34] Thus, to address the above-mentioned knowledge gaps, the novelty of this paper is elucidating the self-healing characteristics of cementitious materials modified with biochar and the effect of biochar on hydration, autogenous shrinkage, and other characteristics of cementitious materials.

In this article, the chemical characteristics and water absorption behavior of biochar are discussed first. Then, the effect of biochar on the early-age properties, autogenous shrinkage, compressive strength, and electrical resistivity of the bulk cement paste was evaluated. Then, the influence of biochar on the chemical characteristics of the healing products as well as the strength recovery and crack filling of cracked cement paste prisms is detailed.

2. MATERIALS AND METHODS

2.1. Materials. *2.1.1. Biochar.* Commercially available biochar derived from wood waste was used in this study. Biochar was characterized using different techniques, including Fourier transform infrared (FTIR) spectroscopy and scanning electron microscopy (SEM) equipped with X-ray energy-dispersive spectroscopy (EDS) to determine the morphology, functional groups, and elemental analysis. Oven-dried biochar was sieved to include biochar particles in the size range of 75−425 μm and then stored in a sealed condition.

2.1.2. Cement Mix Design. In this study, type I/II Portland cement was used to prepare cement pastes. The oxide composition of the cement is provided in Table 1. The designations and mix designs of the cement mixtures are listed in Table 2. The control paste (Ctrl) without biochar had a water/cement ratio (w/c) of 0.3. The cement paste with biochar was produced with a biochar concentration of 2% per cement mass and the same effective w/c of 0.3. The reason for using 2% biochar was based on trials and errors to obtain a paste with acceptable workability and limited negative impact on compressive strength. A lower amount of biochar is expected to limit the potential self-healing effect biochar has in the cement paste. Since biochar absorbed water during cement paste mixing, the amount of absorbed water needs to be estimated and added to the cement mix design to have the same effective w/c in the control paste and the paste with biochar. To determine the biochar absorption, the flow test was performed. In this method, water was incrementally added to the cement paste with biochar, and its flow value was measured until the paste reached the same flow value as that of the control paste. It is assumed that the flow of the paste is governed by the effective w/c of the paste. This method has been used in other investigations for estimating the water absorption of internal curing agents such as hydrogels.[35−42] In the flow test, a cone with dimensions of top diameter = 70 mm, bottom diameter = 100 mm, and height = 50 mm was filled with the cement paste and allowed to sit on a circular metallic tray for 5 min. The cone was then removed, and the tray was lifted and dropped 25 times from a height of 2.5 cm over a period of 15 s with a constant frequency. The two perpendicular diameters of the paste spread were measured, and the average was reported as the flow value. A ZYLA water-reducing admixture at a 0.167% concentration per cement mass was used in the preparation of all pastes. The flow values are shown in Table 2. The added water to the paste with biochar was determined to be w/c = 0.05, making the total w/c of the paste with biochar 0.35.

Table 1. Chemical Compositions of Portland Cement (PC)

composition	%
SiO_2	20.8
Al_2O_3	5.0
Fe_2O_3	3.7
CaO	64.2
MgO	0.9
Na_2O	0.2
K_2O	0.4
SO_3	2.8
TiO_2	0.2

Table 2. Mix Designs and Flow of the Pastes

paste designation	water/cement	superplasticizer (% cement mass)	biochar (% cement mass)	flow (cm)
Ctrl	0.3	0.167	–	20
BC	0.35	0.167	2	20

Biochar and cement were first dry-mixed for 5 min by using a mixer. Then, the cement and biochar were mixed in a plastic bucket with a mixer at a speed of 440 rpm for 30 s. Then, the inside wall of the bucket was scraped and the paste was mixed again for 60 s at a higher speed of 1600 rpm. The paste cubes were cast into the molds of dimensions 50 × 50 × 50 mm per ASTM C 109. The pastes were wrapped with a plastic sheet to prevent water evaporation. After 24 h, the cubes were demolded and placed in a sealed bag for curing.

2.2. Methods. *2.2.1. Biochar Absorption Using the Teabag Test.* The teabag test was utilized for the biochar absorption measurement. The teabag test has been widely used in measuring the absorption of internal curing materials such as hydrogels in construction materials.[39,40,42−4347] To account for the chemistry of the cement paste, the biochar absorption was measured in an artificial cement pore solution. The artificial pore solution was formulated per the procedure described in ref 48. The solution was prepared with 0.1062 M KOH, 0.0489 M Na_2SO_4, 0.037 M K_2SO_4, and 0.0212 M $Ca(OH)_2$. Two g portion of dried biochar was poured in teabags and submerged in the artificial pore solution. At different times, the teabag was gently taken out of the solution and surface-dried with a Kimwipe, and its mass was measured using a balance with a resolution of 0.001 g. The mass of the prewetted empty teabags was also measured. The absorption of biochar, Q, was determined using eq 1:

$$Q = \frac{m_{\text{total}} - m_{\text{wet teabag}} - m_{\text{d bc}}}{m_{\text{d bc}}} \quad (1)$$

where m_{total} is the mass of the wet teabag containing biochar, $m_{\text{wet teabag}}$ is the mass of the empty teabag prewet in the artificial pore solution,

https://doi.org/10.1021/acssuschemeng.4c02045
ACS Sustainable Chem. Eng. 2024, 12, 8261−8275

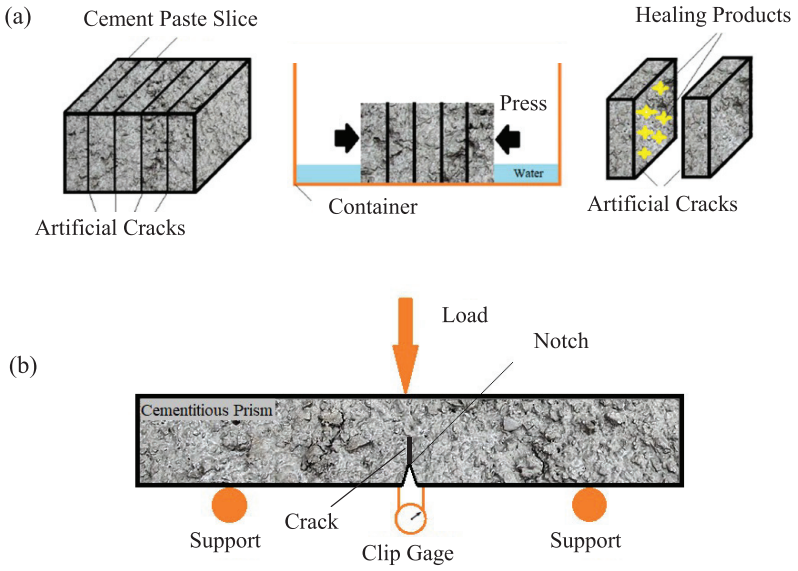

Figure 1. Schematic of (a) the artificial crack healing setup and (b) the three-point bend setup for the crack healing experiments.

and m_{dbc} is the mass of the dry biochar. The experiment was repeated twice, and the average was reported.

2.2.2. X-ray Microcomputed Tomography (Micro-CT). The internal microstructure of the control paste and the paste with biochar was examined by using micro-CT. Twenty-five mm cubes cut from the sample used in the setting time test were scanned in a Bruker Skyscan 1273. The scanning was conducted using a resolution of 20 μm/pixel, an X-ray exposure time of 4300 ms, a rotational step of 0.5°, a current of 115 μA, and a voltage of 130 kV. The CTAnalyzer 1.20.8 was used for the reconstruction and post analysis of a volume with dimensions of 20 × 20 × 20 mm. Since the biochar used had a dry size range of 75−425 μm, the voids smaller than 75 were excluded in the measurement of the biochar voids created in the microstructure due to the biochar water uptake and desorption.

2.2.3. Setting Time. To measure the initial and final setting times of the pastes, a Vicat needle test was employed. The penetration of the Vicat needle was recorded at 30 min time intervals until the initial setting time and at 15 min time intervals until the final setting time. Five separate locations on the paste were probed for this test, and the average was reported.

2.2.4. Isothermal Calorimetry. The heat flow and cumulative heat release were measured by using isothermal calorimetry. Approximately 6 g of the paste was immediately placed in glass ampules. The glass ampules were then sealed with lids to prevent moisture evaporation and monitored in a TA Instruments isothermal calorimeter. Before the start of the measurement, the instrument had been preconditioned at a temperature of 23 °C. Two samples were used for each mix design, and data collection was conducted for more than 72 h.

2.2.5. Autogenous Shrinkage. This test was performed using corrugated polyethylene tubes filled with fresh cement mixtures, as per ASTM C1698-16 at room temperature. Both ends of the tubes (420 mm in length and 29 mm in outer diameter) were sealed with plastic caps, and the variation in the sample length was monitored via a DC linear variable differential transformer (LVDT). Measurements began at the setting time of the cement pastes, carried out twice a day in the first 5 days and continued once a day until 28 days. For each paste, three replicates were used, and the average was reported.

2.2.6. Compressive Strength. The compressive strength of the paste cubes was measured at the ages of 3, 7, and 28 days. Five cubes from each paste were broken at each age using the SATEC machine, and the average strength was reported.

2.2.7. Electrical Resistivity. The electrochemical impedance spectroscopy (EIS) technique was used to measure the electrical resistivity of the paste cubes at the ages of 3, 7, and 28 days. The electrical resistivity provides insight into the transport characteristics of cementitious materials.[3,7,39,40,42,45,47−4849505152535455] To this end, two pieces of foam, presoaked in a 1 M NaCl solution, were inserted between the cube side surfaces and metallic plates. The test was done using a Gamry Reference 600 potentiostat/galvanostat with an AC input of 250 mV and a frequency range of 10^6 to 10 Hz. The test was conducted with five replicates and the average was reported.

2.2.8. Sample Preparation and Characterization of Self-Healing Products. Artificial cracks were used to allow us to obtain healing products in sufficient quantities for the chemical analysis, including thermogravimetric analysis (TGA), FTIR, and SEM/EDS, as used in previous studies.[49] Cement paste cubes with and without biochar with a mixed design described in Table 2 were cast. Cement slices at the age of 7 days with dimensions of 50 × 50 × 15 mm were cut from the cubes using a diamond saw. The slices were then polished with sandpapers of grit sizes of 320, 500, and 1200 using water as a lubricating liquid. The final polishing was done with a 1 μm diamond paste abrasive. The slices were dried in a vacuum oven overnight and then pressed together and partially submerged in water for 2 weeks for the healing process to occur. Figure 1a depicts the setup used in this experiment. The width of the artificial crack was measured to be about 60 μm using a KEYENCE VHX 5000 digital optical microscope. After healing for 2 weeks, the healing products were scratched off from the surface of the slices and vacuum-dried at a temperature of 40 °C for 24 h. Then, the samples were analyzed with TGA, FTIR, and SEM/EDS, as described later. The optical images of the healing products before being scratched off from the cement paste slices were taken.

2.2.9. Thermogravimetric Analysis (TGA). TGA was performed on the bulk pastes at ages of 3, 7, and 28 days and also on the healing products. The sample preparation for the healing products was described above. For the bulk paste, the sample was obtained from the central portion of broken paste cubes used in the compressive strength test. The small pieces of the paste were first immersed in alcohol for 1 day to stop hydration and then vacuum-dried at 50 °C for another day. Then, the samples were ground into powder and passed through the sieve No. 60. The TGA test was conducted using a TA 55 instrument in the temperature range of 25−1000 °C and at the rate of 20 °C/min under N_2 gas. Equations 2 and 3 were used to determine the normalized contents of calcium hydroxide (CH) and calcium carbonate (CC):[50,51]

$$\mathrm{CH} = \frac{74.1}{18}\frac{\bar{M}}{M} \tag{2}$$

https://doi.org/10.1021/acssuschemeng.4c02045
ACS Sustainable Chem. Eng. 2024, 12, 8261−8275

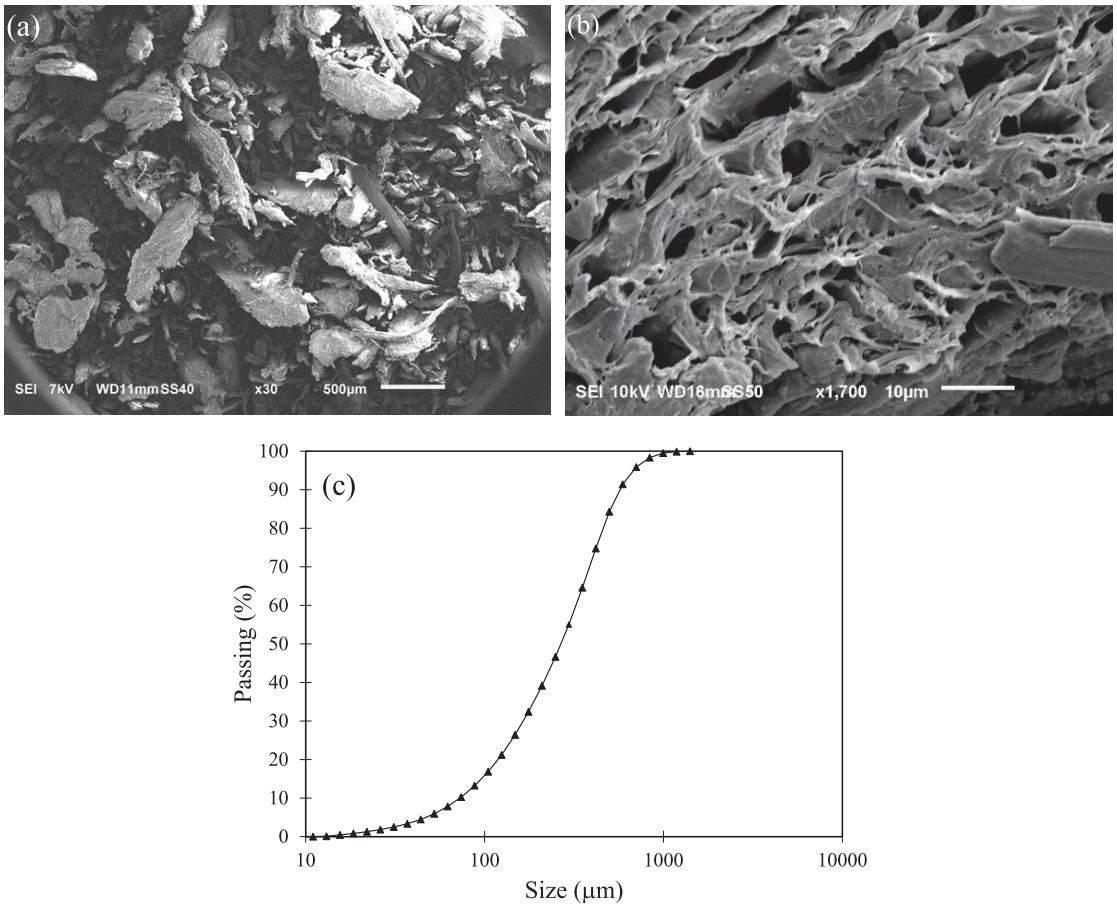

Figure 2. SEM image of biochar particles at (a) low and (b) high magnifications. (c) Particle size distribution of the biochar used in the cement paste.

$$CC = \frac{100}{44}\frac{\bar{M}}{M} \tag{3}$$

where $\bar{M}$ (mg) and M (mg) are the mass change corresponding to the decomposition of CH or CC and the initial mass, respectively.

2.2.10. FTIR Spectroscopy. FTIR spectroscopy was conducted using a PerkinElmer Paragon 1000 FTIR instrument with an ATR accessory. The sample preparation was the same as that for TGA described previously. The samples were scanned in the transmission mode in the range of 600−4000 cm^{-1} at a resolution of 4 cm^{-1}. More than two replicates were used for each paste.

2.2.11. Scanning Electron Microscopy/X-ray-Dispersive Spectroscopy (SEM/EDS). SEM/EDS examination of the healing products was done using a JEOL SEM equipped with an EDS. To avoid charging, samples were gold-coated using a sputter coater. The images were taken at a voltage of 15 kV for the healing products.

2.2.12. Mechanical Strength Recovery. To examine the mechanical strength recovery of the control paste and the paste with biochar, paste prisms with dimensions of 25.4 × 25.4 × 285 mm and with the same mix designs as those shown in Table 2 were cast. First, a notch with a width and depth of 2.0 and 1.5 mm, respectively, was created in the middle of all prisms using a diamond saw. Then, all prisms were precracked using a three-point bend setup at a rate of 0.0002 mm/s in an Instron testing machine (see Figure 1b). During the loading, the crack opening was monitored by using a clip gage. The loading was stopped once a crack width of 0.2 mm was obtained, and then, the prisms were unloaded. After unloading, the crack width of the prisms was measured to be about 60 ± 6 mm by using an optical microscope. It should be noted that in order to increase the ductility of the paste prisms for precrack generation and prevent complete failure of the prisms, 38 mm diameter PVA fibers at a volume percentage of 2% were added to the paste prisms. The cracked prisms were healed by subjecting them to dry/wet cycles, consisting of submersion in water for 1 h and exposure to air (room temperature of 23 °C and relative humidity of 60 ± 5%) for 23 h. The prisms were healed for 28 cycles. After that, the prisms were loaded in a three-point bend setup until complete failure. The strength recovery was determined using eq 4:

$$SR = \frac{P_{max,healing} - P_{unloading}}{P_{max,initial} - P_{unloading}} \times 100\% \tag{4}$$

where $P_{max,initial}$, $P_{max,healing}$, and $P_{unloading}$ are the maximum load obtained during the first loading to generate the initial crack width, the maximum load reached by the healed prisms, and the residual load, corresponding to the load at which the initial predefined crack width was reached, followed by unloading, respectively.

2.2.13. Crack Filling. A KEYENCE VHX 5000 digital optical microscope was employed to investigate the crack filling of the prisms. To this end, both sides of the precracked prisms were imaged at cycles 0, 3, 7, 14, and 28 of healing.

3. RESULTS AND DISCUSSION

3.1. Biochar. *3.1.1. Biochar Characterization.* Figure 2a,b shows the SEM image of biochar particles at low and high magnifications. The particle size distributions of the biochar particles are shown in Figure 2c. The average size of the biochar particles is in the range of 260−270 μm. The porous nature of biochar is evident from the SEM image (Figure 2b) where voids of different sizes are present. These voids are generated due to the decomposition of organic substances in the microstructure of biowaste during the pyrolytic process.

https://doi.org/10.1021/acssuschemeng.4c02045
ACS Sustainable Chem. Eng. 2024, 12, 8261−8275

The presence of macrovoids facilitates transport of water into smaller pores, which are critical to the water uptake capacity of biochar.[7,52] Figure 3 shows the elemental analysis obtained

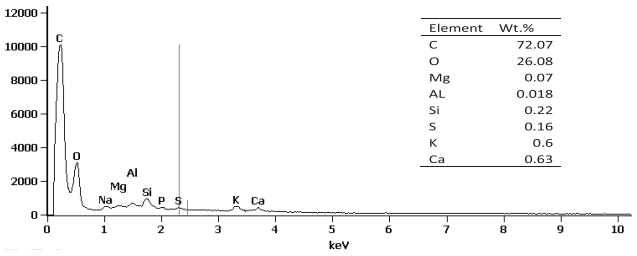

Figure 3. EDS analysis of the biochar used in this study.

from EDS. The EDS spectrum on the surface of BC identified the major elements as carbon (72%) and oxygen (26%). Silicon, calcium, sulfur, potassium, magnesium, and aluminum in very small amounts were also observed.

Figure 4 shows the FTIR spectrum of BC. The BC spectrum presents four significant peaks at wavelengths of 1034, 1602,

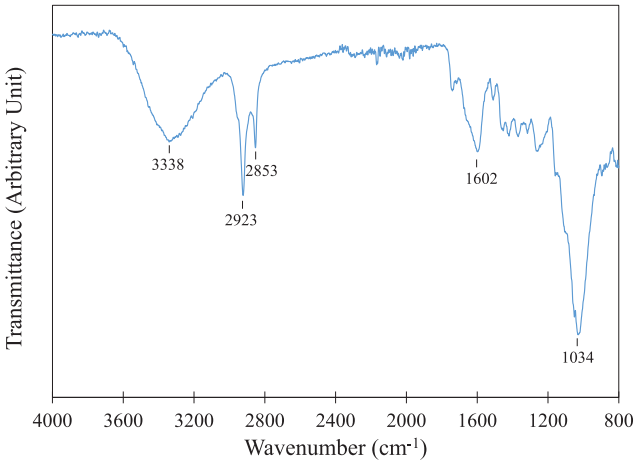

Figure 4. FTIR spectrum of biochar.

2853−2923, and 3338 cm^{-1}. These wavelengths are attributed to carbonyl (C−O), alkene (C═C), alkyl (C−H), and hydroxyl (−OH) groups, respectively.[53] The presence of these functional groups, especially hydroxyl groups, is important in the hydration reaction.

3.1.2. Biochar Absorption. Three parameters, water absorbed and retained in biochar pores, water absorbed on the surface, and water absorbed in the space between biochar particles determine the absorption capacity of biochar, with larger pores retaining a higher amount of water and connecting meso and micropores.[3,,55] Figure 5 illustrates the absorption behavior of biochar, with the biochar size in the range of 75−425 μm, measured using the teabag method in a simulated pore solution to resemble the chemistry of the cement paste. The absorption rate rises sharply in the very first few minutes of the test, reaching a maximum of 6.32 (g/g) at about 5 min. Water uptake by biochar then reached a plateau of 6.2 g/g until the end of the experiment at 60 min. The teabags were left in the solution, and the solution was sealed to avoid carbonation. These were then measured after 24 h, and no significant change in mass was observed. As stated earlier, the added water to the paste with biochar was determined to be w/

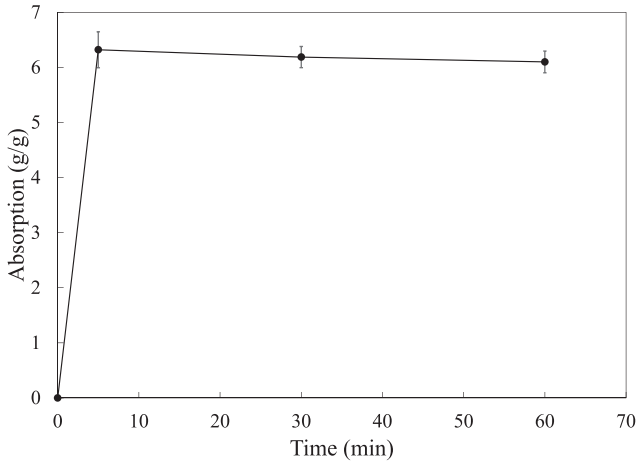

Figure 5. Absorption of biochar with time used in this study.

c = 0.05 using the flow test, which translates to a biochar absorption of 2.5 g/g. The reason for a lower absorption of biochar in the paste obtained from the flow test (2.5 g/g) compared to the absorption obtained from the teabag test in the solution (6.2 g/g) is that in the paste, biochar is constrained by the surrounding cement particles, and also access to the solution is not as readily possible as in the case of the solution where biochar has infinite access to the solution. Since the flow test provides a more realistic absorption of biochar in the cement paste, the absorption results from this test were utilized in the mix designs of the paste.

3.2. Bulk Properties of the Cement Paste. *3.2.1. Micro-CT Analysis.* The two-dimensional (2D) reconstruction images obtained using micro-CT of the internal microstructure of the control paste and the paste with biochar are shown in Figure 6a,b, respectively. A segmented image of Figure 6b is shown in Figure 6c. Black features with spherical morphologies are seen in both images and are attributed to air voids introduced during the mixing of the pastes. Biochar is seen as a dark gray feature with an angular morphology in the microstructure of the paste with biochar only. Table 4 shows the total counts and porosities of the biochar voids. Since biochar with a dry size range of 75−425 μm was used in the paste, voids smaller than 75 μm were excluded. It is noted that the paste with biochar exhibited a larger porosity and void count due to the presence of biochar in this paste. It is also noted that biochar appeared to be well dispersed in the microstructure, and no biochar segregation is observed in the microstructure of the paste with biochar.

3.2.2. Setting Time and Heat of Hydration. Table 3 lists the results of the setting time test. The presence of biochar increased the initial and final setting times of the pastes. The longer setting time in the paste with biochar is due to delayed hydration at an early age in these pastes. The delayed precipitation of hydration products results in slower percolation of the solid skeleton in the microstructure, which prolongs the setting times. It is also plausible that some of the water initially absorbed by biochar was released into the paste, which increased the w/c and interstitial space between the solid skeleton in the microstructure, delaying the setting of the pastes.

The heat flow and cumulative heat evolution of the different pastes are presented in Figure 7a,b, respectively. The results of a paste with a w/c of 0.35 without biochar are also included for

https://doi.org/10.1021/acssuschemeng.4c02045
ACS Sustainable Chem. Eng. 2024, 12, 8261−8275

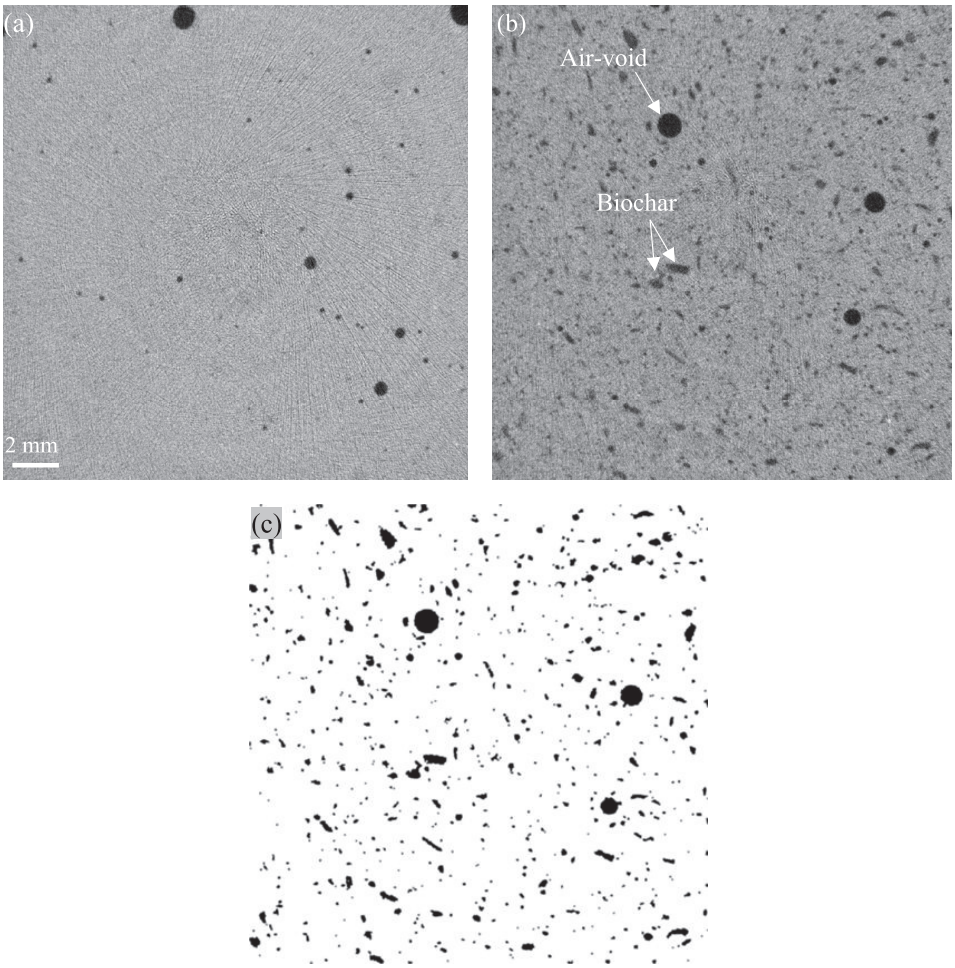

Figure 6. 2D reconstruction of the internal microstructure of (a) the control paste and (b) the paste with biochar. (c) Segmented image of panel (b). Biochar and air voids are seen as black features. The scale bar is the same for all images.

Table 3. Setting Times of Ctrl and BC

sample	initial setting time (min)	final setting time (min)
Ctrl	189	269
BC	417	622

Table 4. Porosity and Count of the Voids Larger than 75 μm in Ctrl and BC Obtained Using Micro-CT

sample	count	total porosity (%)
Ctrl	1927	0.5
BC	15,343	2.81

comparison. The first peak, which appeared in the early stage of hydration, corresponds to cement particle dissolution. The second peak corresponds to the precipitation of binding products, including calcium−silicate−hydrate (C−S−H). It is observed that the second peak had a 12% lower intensity and occurred 4.1 h later in the paste modified with biochar compared to the control paste. In addition, it appears that the induction period of hydration increased in the paste with biochar. A potential reason for the delayed peak of hydration is the uptake of alkalis by biochar during the mixing stage, which resulted in a lower concentration of alkalis in the pore solution and consequently delayed the main peak of hydration.[56,57] It is also plausible that some of the water initially absorbed by biochar was released, which dilutes the ionic concentration in the pore solution, delaying the precipitation of hydration products and laying down the main peak of hydration (Table 4).

Despite the delayed hydration at early hours, the paste with biochar demonstrated a slightly higher cumulative heat release compared with the control paste at later ages. This is attributed to a gradual release of water from biochar into the paste increasing the total w/c and enhancing the hydration reaction at later ages. Another contributing factor is that the large surface area of biochar can act as nucleation sites for the precipitation of cement hydrates. This observation is in agreement with prior studies that showed that the biochar particle size and the wet surface of biochar pores provide favorable conditions for the precipitation of reaction products.[58]

3.2.3. TGA/Derivative Thermogravimetry (DTG). The TGA/DTG curves of the control paste and the paste containing biochar at the age of 28 days are shown in Figure 8a,b. Three decomposition peaks can be seen in the DTG curves. The first peak, occurring between 25 and 200 °C, is associated with the dehydration of calcium aluminate hydrates (C−A−H) and C−S−H gel. The decomposition of calcium hydroxide (CH) occurs at 370−450 °C, while the mass loss corresponding to the decomposition of calcium carbonate takes place between 550 and 750 °C.[59−62] CH is considered an

https://doi.org/10.1021/acssuschemeng.4c02045
ACS Sustainable Chem. Eng. 2024, 12, 8261−8275

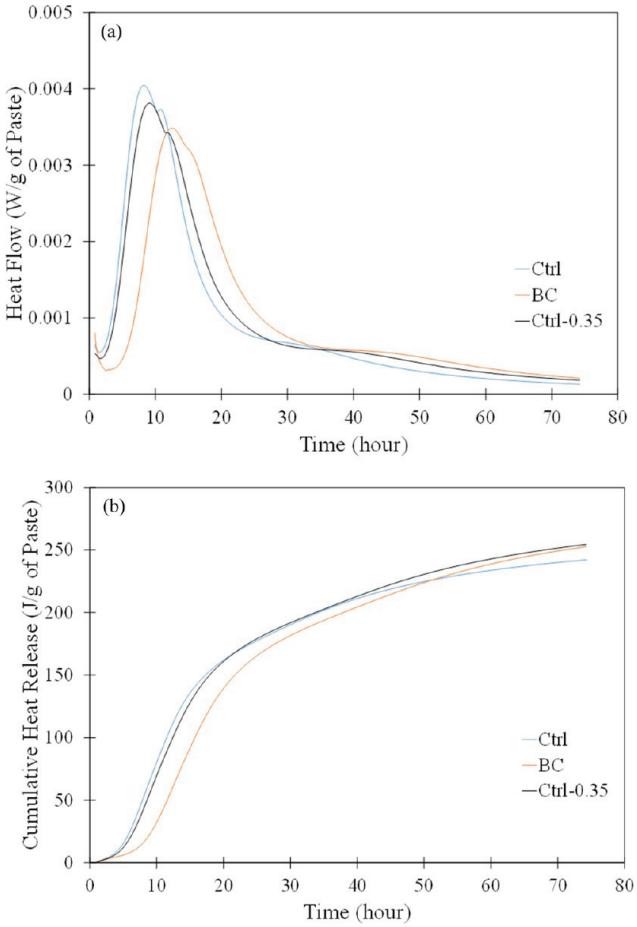

Figure 7. (a) Heat flow and (b) cumulative heat curves of the control paste and the paste with biochar.

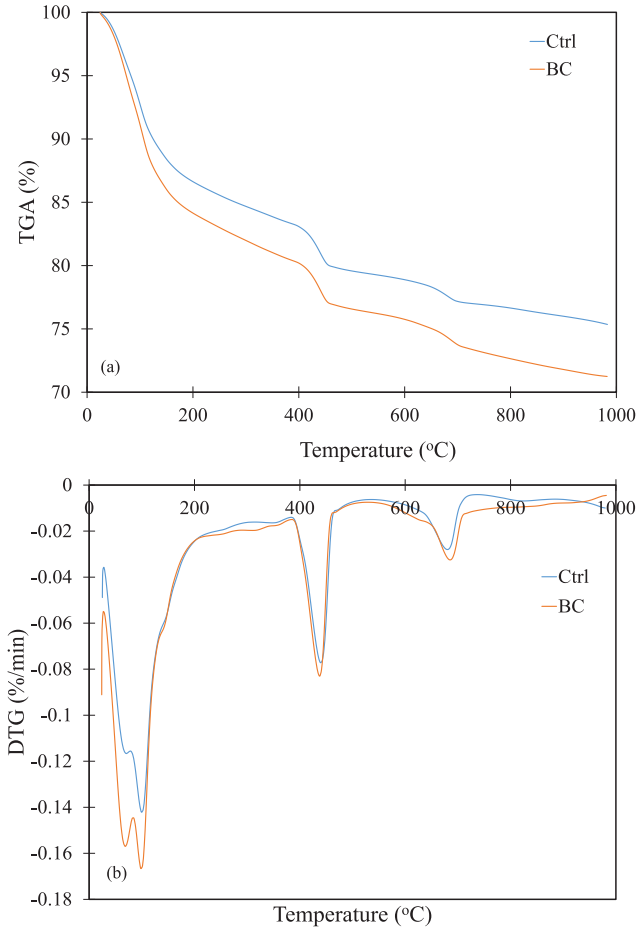

Figure 8. (a) TG and (b) DTG curves of the control paste and the paste with biochar.

important indicator of the hydration degree.[63] Figure 9 illustrates the results of calcium hydroxide (CH) content for both Ctrl and BC at varied ages of 3, 7, and 28 days. The CH content was normalized with respect to the cement paste mass. The paste with biochar showed a CH content relatively similar to that of the control paste in all ages. In light of a delayed early hydration in BC, compared to that in Ctrl, as demonstrated in the heat of hydration results, the relatively similar CH content in both Ctrl and BC points to improved hydration in CH at later ages. The water initially absorbed by biochar is gradually released into the surrounding microstructure, promoting hydration in the microstructure. The effect of biochar on improving hydration in cementitious materials has also been documented in the previous studies.[3,7]

3.2.4. Autogenous Shrinkage. The autogenous shrinkage results of different pastes are shown in Figure 10. The effectiveness of biochar in reducing autogenous shrinkage is evident from this figure. This lower autogenous shrinkage in the biochar-modified paste is attributed to the provision of water from biochar into the surrounding cementitious paste. The relative humidity in the microstructure of the biochar-modified paste is maintained compared to that of the control paste, resulting in a lower capillary action in the pore structure. As discussed earlier, the capillary forces take place in the cementitious matrix due to the gradual drop in the relative humidity, leading to a gradual increase in self-desiccation and autogenous shrinkage. The paste with biochar underwent

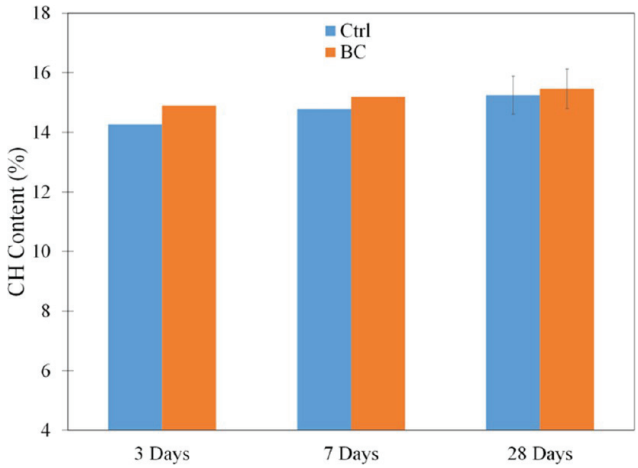

Figure 9. CH content of the control paste and the paste with biochar at different ages.

initial expansions for up to 1.5 days, with the expansion reaching 180.5 m strain, followed by gradual shrinkage over the next 5 days. The paste with biochar then exhibited a small shrinkage for the next 10 days, and its shrinkage remained steady until the age of 28 days. The incorporation of biochar decreased the autogenous shrinkage of cement pastes by 82% with respect to the control cement paste without the addition of biochar.

https://doi.org/10.1021/acssuschemeng.4c02045
ACS Sustainable Chem. Eng. 2024, 12, 8261−8275

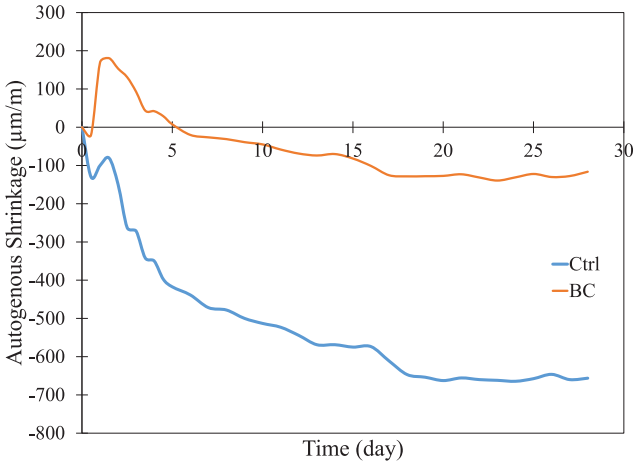

Figure 10. Autogenous shrinkage of the control paste and the paste with biochar at different ages.

3.2.5. Compressive Strength. The results of the compressive strength test at different ages are depicted in Figure 11.

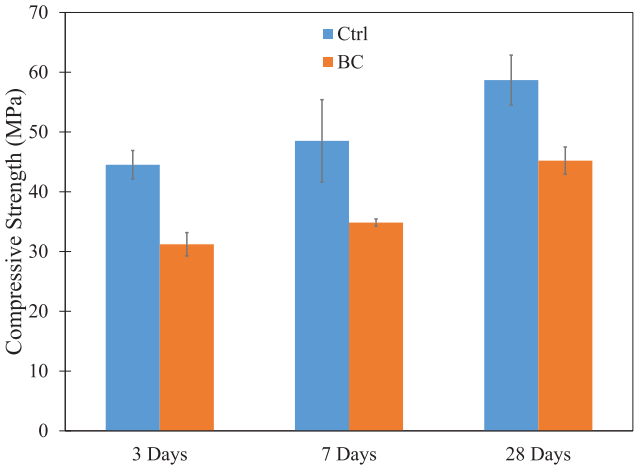

Figure 11. Compressive strength of the control paste and the paste with biochar at different ages.

The paste with biochar exhibited a reduction in compressive strength compared to that of the control paste. It can be observed that the paste with biochar showed a 30% reduction at the age of 3 and 7 days compared to the control paste, while this reduction reaches 23% at the age of 28 days. The decrease in the values of compressive strength is primarily due to the macrovoid formation in the cementitious matrix as a result of the presence of biochar. The biochar macrovoids serve as stress concentration sites in the microstructure of the paste, reducing the load-carrying capacity of the material.[24] This effect of biochar on compressive strength has also been observed in the previous studies.[3,64] However, with continued curing, the compressive strength values of both the control paste and the paste with biochar improved. Although the water released from biochar into the surrounding matrix is expected to improve hydration, the negative impact associated with the presence of biochar macrovoids in the microstructure outweighs the effect of improved hydration.[19,37] It should be pointed out that the effect of biochar on the strength of cementitious materials depends on the mix design used in the preparation of the samples, curing age, and biochar characteristics.[5,65]

3.2.6. Electrical Resistivity. The values of the electrical resistivity at varied ages are shown in Figure 12. Pore solution

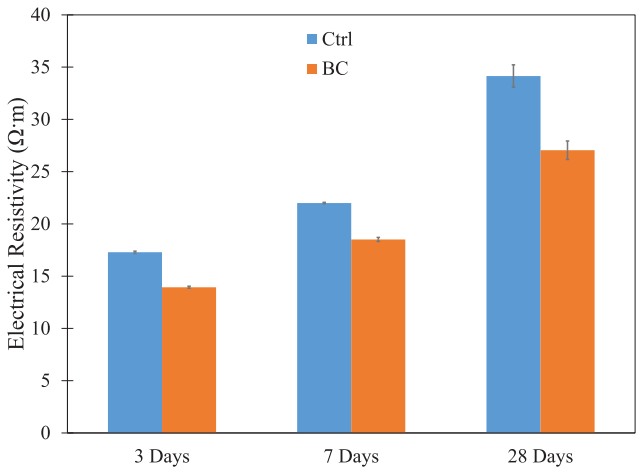

Figure 12. Electrical resistivity of the control paste and the paste with biochar at different ages.

chemistry together with pore morphological characteristics are the factors determining the electrical resistivity in cement pastes.[66−71] As can be seen in Figure 12, the electrical resistivity of both control and biochar-modified pastes increased with age. This improvement in the electrical resistivity with age is attributed to the refinement in the macrostructure due to further hydration. It is seen that the paste with biochar had a reduced electrical resistivity relative to that of the control paste. The higher overall w/c and the consequently less densified microstructure in the paste with biochar compared with the control paste can explain this behavior. Prior investigations have shown an increase in the electrical resistivity with decreasing w/c in cementitious materials.[41,45,68−697071] It should be noted that biochar is electrically conductive, and the addition of them into the cement mixture could contribute to a lower overall electrical resistivity of the paste. The saturation degree of the macrovoids left by biochar is a factor when it comes to the effect of macrovoids on the electrical resistivity. The electrical resistivity of samples decreases if the macrovoids are fully/partially saturated. In this case, they behave as an electrical conductor. On the contrary, macrovoids act as an electrical insulator if they are empty of the pore solution, resulting in an increase in the electrical resistivity.[72] It is expected that the saturation of the macrovoids would be somewhere between the two cases.

3.3. Self-Healing. *3.3.1. Optical Imaging of Healing Products.* The surface of the cement slices after self-healing was observed with an optical microscope. Figure 13 presents the morphology of the healing products after healing for 7 days. Healing products can be observed to have formed as a bluish feature, and the cement slice surface can be observed as a reddish feature in the image. It is evident that the healing products did not cover the entire artificial crack surface. It is noted that the healing products seemed to show a larger surface coverage in the case of BC compared with the control paste. This potentially indicates a higher amount of healing products formed in the case of BC compared to that of the control paste. A whitish phase with a crystal-like morphology is seen in the healing products of the paste with BC. This phase is

https://doi.org/10.1021/acssuschemeng.4c02045
ACS Sustainable Chem. Eng. 2024, 12, 8261−8275

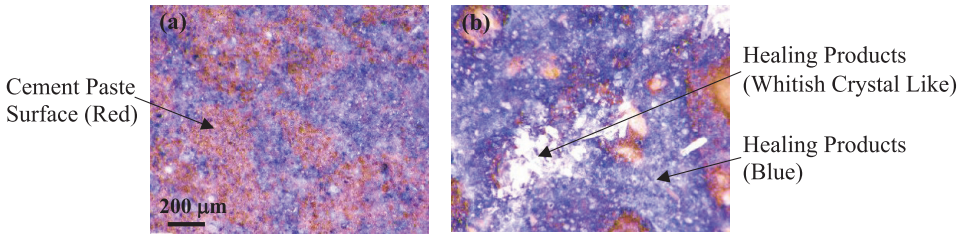

Figure 13. Optical images of the healing products on the surface of (a) the control paste and (b) the paste with biochar. The scale bar is the same for both images. The healing products are shown in blue and whitish crystal-like. The cement paste surface without healing products is shown in red. Optical images are enhanced to improve the visibility of various features.

attributed to calcium carbonate, and their appearance is more pronounced in the paste with BC compared to the control paste. It is postulated that the crystal-like phase tended to form near or at biochar particles embedded in the cementitious matrix, where more water is provided by biochar particles for the carbonation reaction to occur.

3.3.2. TGA/DTG of Healing Products. The TGA/DTG results of the healing products of the control paste and the paste with biochar are shown in Figure 14a,b. It can be observed that similar to the TGA and DTG curves of the bulk control and biochar-modified pastes, three major peaks can be identified in the TGA thermographs of the healing products scratched off from cement paste artificial cracks. The weight loss between 70 and 200 °C is attributed to the loss of chemically bound water of C−S−H and ettringite, and evaporation of free water.[49,61,73,74] However, distinguishing between these phases by TGA/DTG is difficult because they are generally decomposed at a temperature range between 70 and 200 °C.[75] Significant weight losses take place at temperatures ranges of 410−550 and 550−750 °C, with the former being attributed to the decomposition of calcium hydroxide[40,61,76,77] and the latter to the decarbonation of calcium carbonate.[40,59−62,78−81] A slight mass loss is observed at temperatures between 800 and 900 °C, which could be related to the decomposition of calcium carbonate.[82,83] Compared with the bulk cement paste, this peak is more pronounced in the self-healing products.

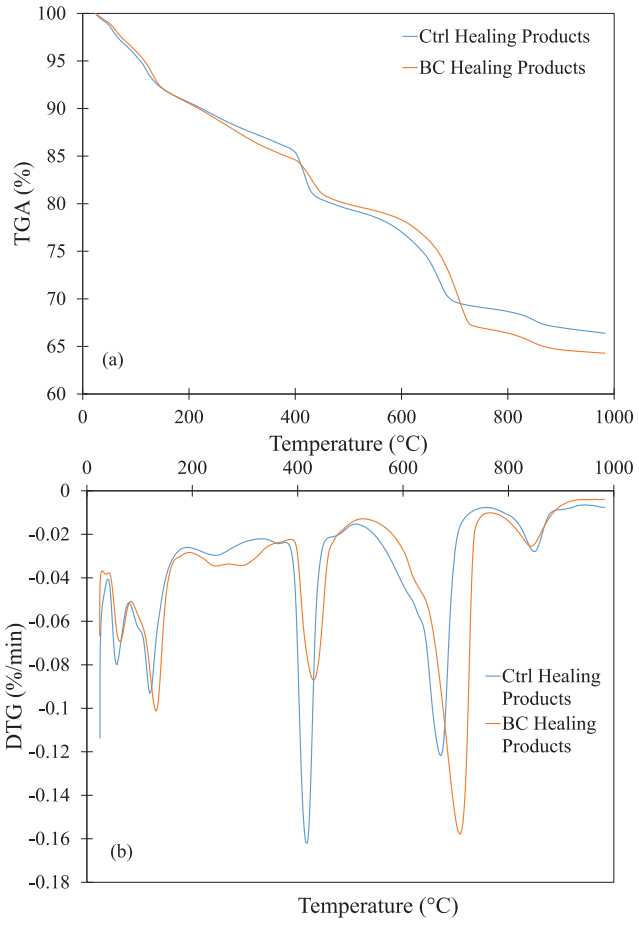

Figure 14. (a) TG and (b) DTG curves of the healing products of the control paste and the paste with biochar.

Once cracks are generated, unhydrated cement particles are exposed on the crack surface. When these unhydrated cement particles on crack surfaces come in contact with water, hydration occurs, and hydration products are formed near the cement particles in the crack space. Ca^{2+} present in the interior of the paste away from the crack surface can diffuse into the crack; the driving force for this diffusion is the lower ionic concentration of Ca^{2+} in the solution in the crack than in the pore solution in the interior of the paste. Since the water that penetrates the crack space is expected to have less ionic species compared to the pore solution in the interior of the paste, such a driving force for Ca^{2+} diffusion is provided. Ca^{2+} can also dissolve from CH present on the surface of the crack into the solution in the crack space; when dissolved CO_2 in the solution in the crack is available, it reacts with Ca^{2+}, resulting in the precipitation of $CaCO_3$.[15,84]

The CH and $CaCO_3$ contents of the healing products of the control paste and the paste with biochar are shown in Figure 15. It is noted that the $CaCO_3$ content is higher in the healing product of the biochar-modified paste compared to that of the control paste. The reason for the increased $CaCO_3$ content in the healing product of BC is the provision of water to the crack surface. Water is critical to the hydration and carbonation reactions. Biochar on the crack surface can retain water or absorb moisture from the environment and gradually release it back to the crack surface in the dry condition, promoting the formation of $CaCO_3$. The lower CH content in the healing products of BC compared to Ctrl is due to the carbonation of CH and its conversion to $CaCO_3$ facilitated by the water provided by biochar, as demonstrated by higher $CaCO_3$ in the healing products of BC compared to that of the control paste. Despite the significantly lower diffusivity of CO_2 in water compared to air, the presence of water is necessary for gaseous CO_2 to react with CH.[85] According to ref 86, CH carbonation takes places in three main steps, starting with dissolution of CH which is the most soluble hydrate.[87] Then, the absorption of carbon dioxide and formation of carbonate ions occur,

https://doi.org/10.1021/acssuschemeng.4c02045
ACS Sustainable Chem. Eng. 2024, 12, 8261−8275

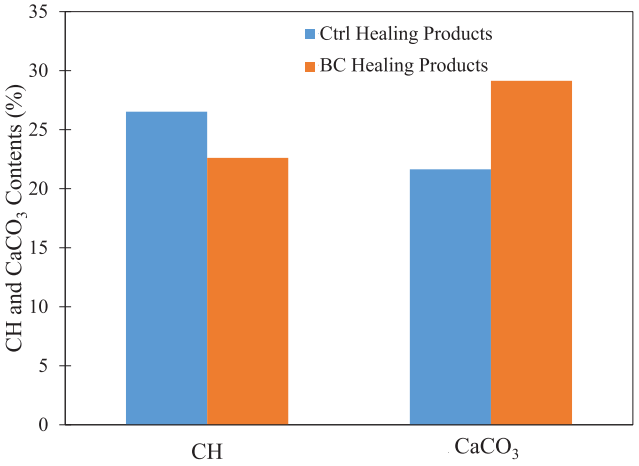

Figure 15. CH and $CaCO_3$ contents of the healing products of the control paste and the paste with biochar.

followed by chemical reaction and precipitation. However, the rate of CH carbonation decreases due to the formation of a thin layer of calcium carbonate on the surface of CH crystals.[88−93]

3.3.3. FTIR Spectroscopy of Healing Products. Figure 16 shows the FTIR spectra of the unhydrated cement, the bulk of

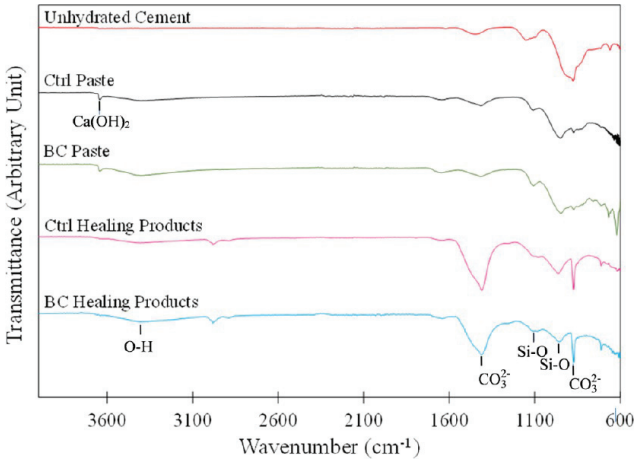

Figure 16. FTIR spectra of the healing products of the control paste and the paste with biochar.

the control and biochar-modified pastes, and the healing products of the control and biochar-modified pastes. A group of bands in the range of 800−1200 cm^{-1} is noted in all spectra; these bands are attributed to the stretching vibration of Si−O bonds.[94] The bands at around 967 and 1110 cm^{-1} in the spectra of the bulk cement pastes and healing products are characteristics of the Si−O stretching vibrations in C−S−H gels.[39,95−98] The band observed at around 1110 cm^{-1} in the bulk paste and healing products can also be attributed to ettringite.[49] The sharp band at 874 cm^{-1} and the broad band at around 1408 cm^{-1} observed more notably in the spectra of the healing products correspond to CO_3^{2-},[95,96] indicating the presence of calcium carbonate. The C−O bending vibration (874 cm^{-1}) and the bands in the range of 1400−1500 cm^{-1} are observed in the spectra of the healing products only and are the characteristic band of CO_3^{2-},[95,96] which can be attributed to the formation of calcium carbonate. The small band at 3640 cm^{-1} noted in the spectra of the bulk paste and healing products is related to the formation of calcium hydroxide.[95] The broad bands at about 3400 and 1640 cm^{-1} are characteristics of the O−H groups in water.[95]

3.3.4. SEM/EDS of Healing Products. The SEM image of the healing products corresponding to Ctrl and BC is shown in Figure 17. Various phases can be seen in the microstructure of

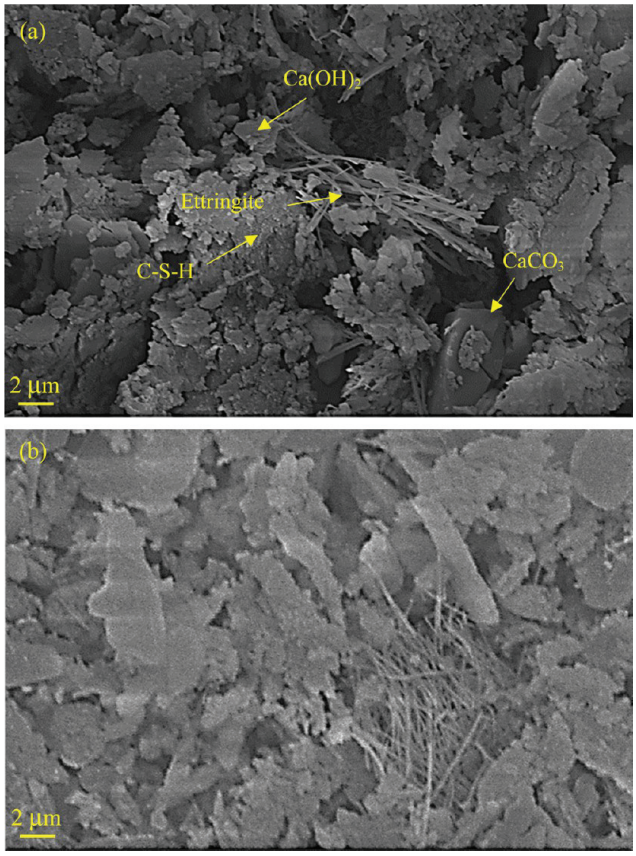

Figure 17. SEM image of the healing products corresponding to (a) Ctrl and (b) BC.

the healing products. The phase with a needlelike morphology is sparsely detected in the microstructure and resembles the morphology of ettringite.[99] The presence of ettringite in small amounts was also found in the FTIR results discussed earlier. It should be noted that the vacuum drying used for the preparation of the sample for chemical characterization could affect the ettringite structure and reduce its content.[100] Platelike crystals are observed, which are attributed to $Ca(OH)_2$. Calcite with a rhombohedral morphology is also evident in the microstructure. The phase with a granular morphology is ascribed to C−S−H. It is noted that the SEM examination of the microstructure of the healing products is in agreement with the FTIR and TGA results. No significant differences in the SEM analysis of the healing products of Ctrl and BC were noted, indicating that the healing products of the two cases comprise similar phases.

The elemental analysis of the healing products corresponding to the control paste and the paste with biochar is discussed in this section. The Ca/Si and Al/Si of the healing products are shown in Figure 18. It is noted the Ca/Si and Al/Si of the healing products in both Ctrl and BC are higher than that of the bulk cement paste. The C−S−H phase produced as a

https://doi.org/10.1021/acssuschemeng.4c02045
ACS Sustainable Chem. Eng. 2024, 12, 8261−8275

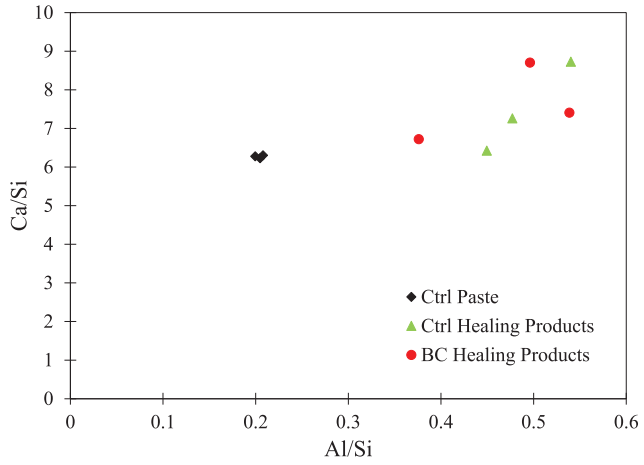

Figure 18. Ca/Si and Al/Ca of the healing products.

result of hydration tends to occupy the space adjacent to the original cement particles and the majority of Si is located in the hydration inner product;[101−103] because the diffusion coefficients of Ca^{2+} and Al^{3+} ions are higher than $H_2 Si_4^{2-}$,[103] the diffusion of Si ions far away from unhydrated cement particles in the bulk paste toward the crack surface is difficult compared to Ca^{2+} and Al^{3+} ions.[49] Therefore, less Si can be found in healing products, leading to relatively higher Ca/Si and Al/Si ratios in the healing products. As shown in Figure 18, the Ca/Si and Al/Si of healing products of BC are relatively similar to that of the Ctrl healing product. It can be concluded that the elemental compositions of the Ctrl and BC healing products are similar.

3.3.5. Strength Recovery. The strength recovery of the Ctrl and BC prisms is presented in Figure 19. It is observed that

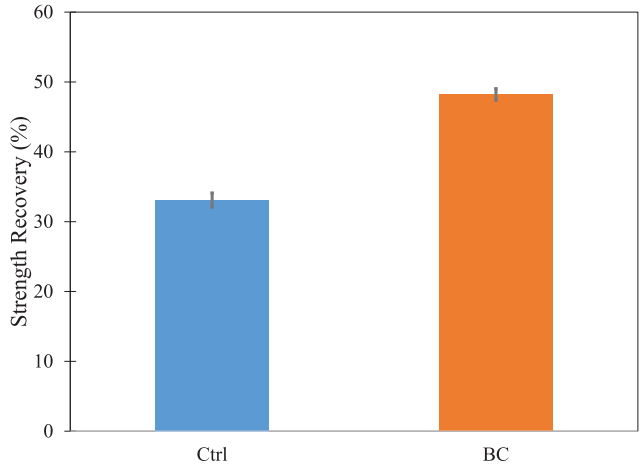

Figure 19. Strength recovery of the control paste and the paste with biochar after healing.

48% of strength was regained in BC, compared to Ctrl, with a strength recovery of 34%, indicating that biochar improved the strength recovery in the cement paste. It should be noted that the observed strength recovery of Ctrl prisms without biochar is ascribed to the intrinsic self-healing behavior in cementitious materials and is comparable with the strength recovery reported in the literature.[84,104] The increase in the strength recovery in BC relative to Ctrl seems to be comparable with some of the prior work using superabsorbent polymers/hydrogels.[106]

Water plays an essential role in the reactions involved in the self-healing process. Water is needed for both hydration and calcium carbonate precipitation reactions. Similar to superabsorbent polymers, biochar is capable of absorbing water and moisture from the surrounding environment. The voids created due to the addition of biochar in the material serve as stress concentration sites in the microstructure, providing a preferential crack pathway where the crack passes through these voids that contain biochar. Thus, biochar is expected to be present on the crack surface. As detailed previously, during the healing process, the cracked prisms, both Ctrl and BC, are subjected to wet/dry cycles. In BC, water is absorbed and retained by biochar particles on the crack surface during the wet periods and released slowly into the crack during the dry periods, resulting in the provision of more water for the further reaction of unreacted cementitious particles available on the crack surface and further calcium carbonate precipitation. Figure 20 demonstrates this process.

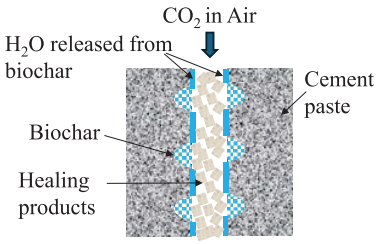

Figure 20. Schematic showing the contribution of biochar to the formation of healing products.

3.3.6. Crack Filling. The optical images taken with optical microscopy showing the crack filling process in the control paste and the paste with biochar at 0, 3, 7, 14, and 28 days are shown in Figure 21. The filling products are seen as a whitish phase in the crack space. It is noted that Ctrl showed increased

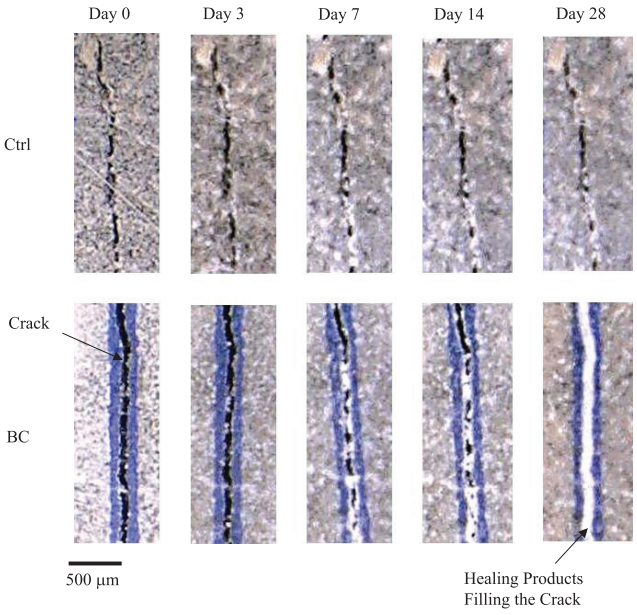

Figure 21. Optical images showing the crack filling in the control paste and the paste with biochar as a function of time.

https://doi.org/10.1021/acssuschemeng.4c02045
ACS Sustainable Chem. Eng. 2024, 12, 8261−8275

crack filling with time; however, only partial filling was achieved up to 28 days. BC showed insignificant crack filling at 3 days, but gradually increased its crack filling at 7 days, reaching complete crack filling by 28 days. Even though the initial crack generation process was the same in both prisms, it is noted that BC appeared to have a larger crack width compared to Ctrl; however, BC was still able to show complete crack filling compared to Ctrl. The effect of biochar in increasing the amount of healing products in the crack seems to be consistent with the results of the optical imaging discussed in Section 3.1.1 and shown in Figure 13. It was noted in Figure 13 that BC demonstrated a larger coverage of the artificial crack surface with the healing products compared to Ctrl. The crack filling and strength recovery results discussed above clearly demonstrate an improvement in the self-healing performance of the paste when biochar is added. While the higher content of the healing products and calcium carbonate seems to correlate with increased self-healing, further investigations are needed to examine the micromechanical characteristics responsible for increased strength recovery in the case of BC.

4. CONCLUSIONS

The self-healing, fresh properties, hydration, and autogenous shrinkage of the cement paste with biochar were investigated. The conclusions are as follows:

- The paste with biochar showed increased initial and final setting times relative to the control paste due to delayed hydration at an early age, as evidenced from isothermal calorimetry. The delayed hydration is due to the absorption of alkali by biochar during the initial stage, which reduced alkali concentrations in the pore solution delaying hydration at an early age. Nevertheless, at later ages, the cement paste with biochar demonstrated a slightly higher hydration heat compared to the control paste due to the release of water from biochar into the surrounding matrix.
- Biochar effectively decreased autogenous shrinkage, which is attributed to the internal curing effect of biochar in the cement paste.
- The cement paste with biochar had a reduced compressive strength and electrical resistivity relative to the control paste. The lower compressive strength is due to the presence of macrovoids created from biochar absorption and desorption. The decrease in the electrical resistivity is due to the higher overall w/c in the paste with biochar relative to the control paste.
- The healing products of the control paste and the paste with biochar consisted of C−S−H, calcium carbonate, CH, and ettringite, as evidenced from TGA, FTIR, and SEM. The calcium carbonate content in the healing products of the paste with biochar was larger than that of the control paste.
- The paste with biochar demonstrated an improved mechanical strength recovery and crack filling relative to the control paste. This is attributed to the ability of biochar to provide water as a key ingredient necessary for the chemical reactions that yield healing products in cracks.

AUTHOR INFORMATION

Corresponding Author

Ali Ghahremaninezhad − *Department of Civil and Architectural Engineering, University of Miami, Coral Gables, Florida 33146, United States;* orcid.org/0000-0001-9269-801X; Phone: (+1) 305-2843465; Email: a.ghahremani@miami.edu

Author

Babak Vafaei − *Department of Civil and Architectural Engineering, University of Miami, Coral Gables, Florida 33146, United States*

Complete contact information is available at: https://pubs.acs.org/10.1021/acssuschemeng.4c02045

Notes

The authors declare no competing financial interest.

ACKNOWLEDGMENTS

This study was supported by the National Science Foundation under the CAREER Award Number 1846984 and the MRI Award Number 1920127 and by the Office of Naval Research under the Award Number N000142212554. Any opinions, findings, and conclusions or recommendations expressed in this material are those of the author(s) and do not necessarily reflect the views of the National Science Foundation or the Office of Naval Research. Sadegh Tale Masoule helped with the micro-CT analysis and is acknowledged.

REFERENCES

(1) Worrell, E.; Price, L.; Martin, N.; Hendriks, C.; Meida, L. O. CARBONDIOXIDE EMISSIONS FROM THE GLOBAL CEMENT INDUSTRY. *Annu. Rev. Energy Environ.* **2001**, *26*, 303−329.

(2) Baffoe, E.; Ghahremaninezhad, A. Effect of Proteins on the Mineralization, Microstructure and Mechanical Properties of Carbonation Cured Calcium Silicate. *Cem. Concr. Compos.* **2023**, *141*, No. 105121.

(3) Dixit, A.; Gupta, S.; Pang, S. D.; Kua, H. W. Waste Valorisation Using Biochar for Cement Replacement and Internal Curing in Ultra-High Performance Concrete. *J. Cleaner Prod.* **2019**, *238*. 117876.

(4) Gupta, S.; Kua, H. W.; Koh, H. J. Application of Biochar from Food and Wood Waste as Green Admixture for Cement Mortar. *Sci. Total Environ.* **2018**, *619−620*, 419−435.

(5) Gupta, S.; Kua, H. W.; Low, C. Y. Use of Biochar as Carbon Sequestering Additive in Cement Mortar. *Cem. Concr. Compos.* **2018**, *87*, 110−129.

(6) Khushnood, R. A.; Ahmad, S.; Restuccia, L.; Spoto, C.; Jagdale, P.; Tulliani, J. M.; Ferro, G. A. Carbonized Nano/Microparticles for Enhanced Mechanical Properties and Electromagnetic Interference Shielding of Cementitious Materials. *Front. Struct. Civil Eng.* **2016**, *10* (2), 209−213.

(7) Choi, W. C.; Do Yun, H.; Lee, J. Y. Mechanical Properties of Mortar Containing Bio-Char from Pyrolysis. *J. Korea Inst. Struct. Maint. Insp.* **2012**, *16* (3), 67−74.

(8) Restuccia, L.; Ferro, G. A. Nano-Particles from Food Waste: A "Green" Feature for Traditional Building Materials. In *9th International Conference on Fracture Mechanics of Concrete and Concrete Structures*; Berkeley: United States, 2016; pp 1−6.

(9) Reinhardt, H. W.; Jooss, M. Permeability and Self-Healing of Cracked Concrete as a Function of Temperature and Crack Width. *Cem. Concr. Res.* **2003**, *33* (7), 981−985.

(10) Gupta, S.; Kua, H. W.; Pang, S. D. Healing Cement Mortar by Immobilization of Bacteria in Biochar: An Integrated Approach of Self-Healing and Carbon Sequestration. *Cem. Concr. Compos.* **2018**, *86*, 238−254.

(11) De Muynck, W.; Cox, K.; De Belie, N.; Verstraete, W. Bacterial Carbonate Precipitation as an Alternative Surface Treatment for Concrete. *Constr. Build. Mater.* **2008**, *22* (5), 875−885, DOI: 10.1016/j.conbuildmat.2006.12.011.
(12) Van Tittelboom, K.; De Belie, N. Self-Healing in Cementitious Materials—a Review. *Materials* **2013**, *6* (6), 2182−2217.
(13) Snoeck, D. Autogenous Healing in 10-Years Aged Cementitious Composites Using Microfibers and Superabsorbent Polymers. *Infrastructures* **2022**, *7* (10). 129.
(14) Snoeck, D.; De Belie, N. Autogenous Healing in Strain-Hardening Cementitious Materials with and without Superabsorbent Polymers: An 8-Year Study. *Front Mater.* **2019**, *6*, 48 DOI: 10.3389/fmats.2019.00048.
(15) Snoeck, D.; De Belie, N. Repeated Autogenous Healing in Strain-Hardening Cementitious Composites by Using Superabsorbent Polymers. *J. Mater. Civil Eng.* **2016**, *28* (1), No. 04015086.
(16) Snoeck, D.; Pel, L.; De Belie, N. Autogenous Healing in Cementitious Materials with Superabsorbent Polymers Quantified by Means of NMR. *Sci. Rep.* **2020**, *10* (1), No. 642, DOI: 10.1038/s41598-020-57555-0.
(17) Baffoe, E.; Ghahremaninezhad, A. On the Interaction between Proteins and Cracked Cementitious Surface. *Constr. Build. Mater.* **2022**, *352* (August), No. 128982.
(18) Baffoe, E.; Ghahremaninezhad, A. The Effect of Biomolecules on Enzyme-Induced Calcium Carbonate Precipitation in Cementitious Materials. *Constr. Build. Mater.* **2022**, *345* (July), No. 128323.
(19) Schröfl, C.; Erk, K. A.; Siriwatwechakul, W.; Wyrzykowski, M.; Snoeck, D. Recent Progress in Superabsorbent Polymers for Concrete. *Cem. Concr. Res.* **2022**, *151* (October 2021), No. 106648.
(20) Wu, M.; Johannesson, B.; Geiker, M. A Review: Self-Healing in Cementitious Materials and Engineered Cementitious Composite as a Self-Healing Material. *Constr. Build. Mater.* **2012**, *28* (1), 571−583.
(21) Homma, D.; Mihashi, H.; Nishiwaki, T. Self-Healing Capability of Fibre Reinforced Cementitious Composites. *J. Adv. Concr. Technol.* **2009**, *7* (2), 217−228.
(22) Li, M.; Li, V. C. Cracking and Healing of Engineered Cementitious Composites under Chloride Environment. *ACI Mater. J.* **2011**, *108* (3), 333−340.
(23) Neville, A. Autogenous Healing—a Concrete Miracle? *Concr. Int.* **2002**, *24* (11), 76−82.
(24) ter Heide, N.; Schlangen, E.Self-Healing of Early Age Cracks in Concrete. In *First International Conference on Self Healing Materials* 2007; pp 1−12.
(25) Lefever, G.; Snoeck, D.; Aggelis, D. G.; de Belie, N.; van Vlierberghe, S.; van Hemelrijck, D. Evaluation of the Self-Healing Ability of Mortar Mixtures Containing Superabsorbent Polymers and Nanosilica. *Materials* **2020**, *13* (2). 380.
(26) Hong, G.; Song, C.; Choi, S. Autogenous Healing of Early-Age Cracks in Cementitious Materials by Superabsorbent Polymers. *Materials* **2020**, *13* (3). 690.
(27) Farzanian, K.; Ghahremaninezhad, A. On the Interaction between Superabsorbent Hydrogels and Blended Mixtures with Supplementary Cementitious Materials. *Adv. Civil Eng. Mater.* **2018**, *7*, 567−589.
(28) Farzanian, K.; Ghahremaninezhad, A. On the Effect of Chemical Composition on the Desorption of Superabsorbent Hydrogels in Contact with a Porous Cementitious Material. *Gels* **2018**, *4* (3), 70.
(29) Farzanian, K.; Ghahremaninezhad, A. Desorption of Superabsorbent Hydrogels with Varied Chemical Compositions in Cementitious Materials. *Mater. Struct.* **2018**, *51* (1), No. 3.
(30) Farzanian, K.; Ghahremaninezhad, A. The Effect of the Capillary Forces on the Desorption of Hydrogels in Contact with a Porous Cementitious Material. *Mater. Struct.* **2017**, *50* (5), No. 216.
(31) Kua, H. W.; Gupta, S.; Aday, A. N.; Srubar, W. V. Biochar-Immobilized Bacteria and Superabsorbent Polymers Enable Self-Healing of Fiber-Reinforced Concrete after Multiple Damage Cycles. *Cem. Concr. Compos.* **2019**, *100* (February), 35−52.
(32) Mo, L.; Fang, J.; Huang, B.; Wang, A.; Deng, M. Combined Effects of Biochar and MgO Expansive Additive on the Autogenous Shrinkage, Internal Relative Humidity and Compressive Strength of Cement Pastes. *Constr. Build. Mater.* **2019**, *229*. 116877.
(33) Dixit, A.; Verma, A.; Pang, S. D. Dual Waste Utilization in Ultra-High Performance Concrete Using Biochar and Marine Clay. *Cem. Concr. Compos.* **2021**, *120*. 104049.
(34) Prabahar, J.; Vafaei, B.; Baffoe, E.; Ghahremaninezhad, A. The Effect of Biochar on the Properties of Alkali-Activated Slag Pastes. *Constr. Mater.* **2022**, *2* (1), 1−14.
(35) Sun, B.; Wu, H.; Song, W.; Li, Z.; Yu, J. Design Methodology and Mechanical Properties of Superabsorbent Polymer (SAP) Cement-Based Materials. *Constr. Build. Mater.* **2019**, *204*, 440−449.
(36) Ma, X.; Liu, J.; Wu, Z.; Shi, C. Effects of SAP on the Properties and Pore Structure of High Performance Cement-Based Materials. *Constr. Build. Mater.* **2017**, *131*, 476−484.
(37) El-Dieb, A. S.; Taha, M. M. R. Flow Characteristics and Acceptance Criteria of Fiber-Reinforced Self-Compacted Concrete (FR-SCC). *Constr. Build. Mater.* **2012**, *27* (1), 585−596.
(38) Prabahar, J.; Vafaei, B.; Ghahremaninezhad, A. The Effect of Hydrogels with Different Chemical Compositions on the Behavior of Alkali-Activated Slag Pastes. *Gels* **2022**, *8* (11), 731.
(39) Vafaei, B.; Farzanian, K.; Ghahremaninezhad, A. Effect of Hydrogels Containing Nanosilica on the Properties of Cement Pastes. *J. Compos. Sci.* **2021**, *5* (4), 105.
(40) Farzanian, K.; Vafaei, B.; Ghahremaninezhad, A. The Influence of the Chemical Composition of Hydrogels on Their Behavior in Cementitious Materials. *Mater. Struct* **2021**, *54* (6), No. 244, DOI: 10.1617/s11527-021-01838-z.
(41) Vafaei, B.; Farzanian, K.; Ghahremaninezhad, A. The Influence of Superabsorbent Polymer on the Properties of Alkali-Activated Slag Pastes. *Constr. Build. Mater.* **2020**, *236*, No. 117525.
(42) Farzanian, K.; Vafaei, B.; Ghahremaninezhad, A. The Behavior of Superabsorbent Polymers (SAPs) in Cement Mixtures with Glass Powders as Supplementary Cementitious Materials. *Materials* **2019**, *12* (21). 3597.
(43) Schröfl, C.; Mechtcherine, V.; Gorges, M. Relation between the Molecular Structure and the Efficiency of Superabsorbent Polymers (SAP) as Concrete Admixture to Mitigate Autogenous Shrinkage. *Cem. Concr. Res.* **2012**, *42* (6), 865−873.
(44) Zhu, Q.; Barney, C. W.; Erk, K. A. Effect of Ionic Crosslinking on the Swelling and Mechanical Response of Model Superabsorbent Polymer Hydrogels for Internally Cured Concrete. *Mater. Struct.* **2015**, *48*, 2261−2276.
(45) Farzanian, K.; Pimenta Teixeira, K.; Perdiago Rocha, I.; De Sa Carneiro, L.; Ghahremaninezhad, A. The Mechanical Strength, Degree of Hydration, and Electrical Resistivity of Cement Pastes Modified with Superabsorbent Polymers. *Constr. Build. Mater.* **2016**, *109*, 156−165.
(46) Kamali, M.; Ghahremaninezhad, A. An Investigation into the Influence of Superabsorbent Polymers on the Properties of Glass Powder Modified Cement Pastes. *Constr. Build. Mater.* **2017**, *149*, 236−247.
(47) Baffoe, E.; Ghahremaninezhad, A. Effect of Hydrogel on Mitigating Drying Shrinkage Induced Cracking in Carbonation Cured Calcium Silicate Binders. *Constr. Build. Mater.* **2024**, *411*, No. 134243.
(48) Tunstall, L. E.; Scherer, G. W.; Prud'homme, R. K. Studying AEA Interaction in Cement Systems Using Tensiometry. *Cem. Concr. Res.* **2017**, *92*, 29−36.
(49) Huang, H.; Ye, G.; Damidot, D. Characterization and Quantification of Self-Healing Behaviors of Microcracks Due to Further Hydration in Cement Paste. *Cem. Concr. Res.* **2013**, *52*, 71−81.
(50) Kim, T.; Olek, J. Effects of Sample Preparation and Interpretation of Thermogravimetric Curves on Calcium Hydroxide in Hydrated Pastes and Mortars. *Transp. Res. Rec.* **2012**, *2290* (2290), 10−18.
(51) Bazhuni, M. F.; Kamali, M.; Ghahremaninezhad, Ali. An Investigation into the Properties of Ternary and Binary Cement

Pastes Containing Glass Powder. *Front. Struct. Civil Eng.* **2019**, *13*, 741−750.
(52) Gupta, S.; Kua, H. W. Effect of Water Entrainment by Pre-Soaked Biochar Particles on Strength and Permeability of Cement Mortar. *Constr. Build. Mater.* **2018**, *159*, 107−125.
(53) Praneeth, S.; Saavedra, L.; Zeng, M.; Dubey, B. K.; Sarmah, A. K. Biochar Admixtured Lightweight, Porous and Tougher Cement Mortars: Mechanical, Durability and Micro Computed Tomography Analysis. *Sci. Total Environ.* **2021**, *750*, No. 142327.
(54) Weber, K.; Quicker, P. Properties of Biochar. *Fuel* **2018**, *217*, 240−261.
(55) Zhang, J.; You, C. Water Holding Capacity and Absorption Properties of Wood Chars. *Energy Fuels* **2013**, *27* (5), 2643−2648.
(56) Justs, J.; Wyrzykowski, M.; Winnefeld, F.; Bajare, D.; Lura, P. Influence of Superabsorbent Polymers on Hydration of Cement Pastes with Low Water-to-Binder Ratio. *J. Therm. Anal. Calorim.* **2014**, *115* (1), 425−432.
(57) Danielson, U. Heat of Hydration of Cement as Affected by Water-Cement Ratio. In *Fourth International Symposium of the Chemistry of Cement*, Washington DC, 1960.
(58) Ali, D.; Agarwal, R.; Hanifa, M.; Rawat, P.; Paswan, R.; Rai, D.; Tyagi, I.; Srinivasarao Naik, B.; Pippal, A. Thermo-Physical Properties and Microstructural Behaviour of Biochar-Incorporated Cementitious Material. *J. Build. Eng.* **2023**, *64*. 105695.
(59) Tobón, J.; Payá, J. J.; Borrachero, Mv.; Restrepo, O. J. Mineralogical Evolution of Portland Cement Blended with Silica Nanoparticles and Its Effect on Mechanical Strength. *Constr. Build. Mater.* **2012**, *36*, 736−742.
(60) Senff, L.; Labrincha, J. A.; Ferreira, V. M.; Hotza, D.; Repette, W. L. Effect of Nano-Silica on Rheology and Fresh Properties of Cement Pastes and Mortars. *Constr. Build. Mater.* **2009**, *23* (7), 2487−2491.
(61) Esteves, L. P. On the Hydration of Water-Entrained Cement−Silica Systems: Combined SEM, XRD and Thermal Analysis in Cement Pastes. *Thermochim. Acta* **2011**, *518* (1−2), 27−35.
(62) Ashraf, M.; Khan, A. N.; Ali, Q.; Mirza, J.; Goyal, A.; Anwar, A. M. Physico-Chemical, Morphological and Thermal Analysis for the Combined Pozzolanic Activities of Minerals Additives. *Constr. Build. Mater.* **2009**, *23* (6), 2207−2213.
(63) Wang, L.; Chen, L.; Tsang, D. C. W.; Guo, B.; Yang, J.; Shen, Z.; Hou, D.; Ok, Y. S.; Poon, C. S. Biochar as Green Additives in Cement-Based Composites with Carbon Dioxide Curing. *J. Cleaner Prod.* **2020**, *258*, No. 120678.
(64) Gupta, S.; Kua, H. W.; Dai Pang, S. Biochar-Mortar Composite: Manufacturing, Evaluation of Physical Properties and Economic Viability. *Constr. Build. Mater.* **2018**, *167*, 874−889.
(65) Li, Z.; Xue, W.; Zhou, W. Mechanical Properties of Concrete with Different Carya Cathayensis Peel Biochar Additions. *Sustainability* **2023**, *15* (6), 4874.
(66) Snyder, K. A.; Ferraris, C.; Martys, N. S.; Garboczi, E. J. Using Impedance Spectroscopy to Assess the Viability of the Rapid Chloride Test for Determining Concrete Conductivity. *J. Res. Natl. Inst. Stand. Technol.* **2000**, *105* (4), 497.
(67) Neithalath, N.; Weiss, J.; Olek, J. *Predicting the Permeability of Pervious Concrete (Enhanced Porosity Concrete) from Non-Destructive Electrical Measurements*; Purdue University: United States, 2006.
(68) Jain, J.; Neithalath, N. Electrical Impedance Analysis Based Quantification of Microstructural Changes in Concretes Due to Non-Steady State Chloride Migration. *Mater. Chem. Phys.* **2011**, *129* (1−2), 569−579.
(69) Neithalath, N.; Weiss, J.; Olek, J. Characterizing Enhanced Porosity Concrete Using Electrical Impedance to Predict Acoustic and Hydraulic Performance. *Cem. Concr. Res.* **2006**, *36* (11), 2074−2085.
(70) Bu, Y.; Weiss, J. The Influence of Alkali Content on the Electrical Resistivity and Transport Properties of Cementitious Materials. *Cem. Concr. Compos.* **2014**, *51*, 49−58.
(71) Rajabipour, F.; Sant, G.; Weiss, J.Development of Electrical Conductivity-Based Sensors for Health Monitoring of Concrete Materials. In *TRB Annual Conference* 2007; p 16.
(72) Wong, H. S.; Pappas, A. M.; Zimmerman, R. W.; Buenfeld, N. R. Effect of Entrained Air Voids on the Microstructure and Mass Transport Properties of Concrete. *Cem. Concr. Res.* **2011**, *41* (10), 1067−1077.
(73) Lothenbach, B.; Le Saout, G.; Haha, M. B.; Figi, R.; Wieland, E. Hydration of a Low-Alkali CEM III/B−SiO2 Cement (LAC). *Cem. Concr. Res.* **2012**, *42* (2), 410−423.
(74) Hall, C.; Barnes, P.; Billimore, A. D.; Jupe, A. C.; Turrillas, X. Thermal Decomposition of Ettringite Ca6[Al(OH)6]2(SO4)3·26H2O. *J. Chem. Soc., Faraday Trans.* **1996**, *92* (12), 2125−2129.
(75) Snoeck, D.; Jensen, O. M.; de Belie, N. The Influence of Superabsorbent Polymers on the Autogenous Shrinkage Properties of Cement Pastes with Supplementary Cementitious Materials. *Cem. Concr. Res.* **2015**, *74*, 59−67.
(76) Ye, G.; Liu, X.; de Schutter, G.; Poppe, A.-M.; Taerwe, L. Influence of Limestone Powder Used as Filler in SCC on Hydration and Microstructure of Cement Pastes. *Cem. Concr. Compos.* **2007**, *29* (2), 94−102.
(77) Pane, I.; Hansen, W. Investigation of Blended Cement Hydration by Isothermal Calorimetry and Thermal Analysis. *Cem. Concr. Res.* **2005**, *35* (6), 1155−1164.
(78) Wu, L.; Zhang, Z.; Yang, M.; Yuan, J.; Li, P.; Men, X. Graphene Enhanced and in Situ-Formed Alginate Hydrogels for Reducing Friction and Wear of Polymers. *Colloids Surf., A* **2020**. *589*124434.
(79) Baffoe, E.; Ghahremaninezhad, A. Crack Binding and Filling Properties of Modified Proteins in Sustainable Cementitious Materials. *ACS Appl. Eng. Mater.* **2023**, *1* (10), 2685−2697.
(80) Vafaei, B.; Ghahremaninezhad, A. Investigating the Effect of Hydrogel Characteristics on the Self-Healing of Cementitious Materials. *Mater. Struct.* **2023**, *56* (10), No. 177, DOI: 10.1617/s11527-023-02265-y.
(81) Baffoe, E.; Dauer, E.; Ghahremaninezhad, A. Effect of Proteins on Biocementation in Construction Materials. *iScience* **2024**, *27* (1), No. 108743.
(82) Thongsanitgarn, P.; Wongkeo, W.; Chaipanich, A. Hydration and Compressive Strength of Blended Cement Containing Fly Ash and Limestone as Cement Replacement. *J. Mater. Civil Eng.* **2014**, *26* (12), No. 04014088.
(83) Mitchell, L. D.; Margeson, J. The Effects of Solvents on C−S−H as Determined by Thermal Analysis. *J. Therm. Anal. Calorim.* **2006**, *86* (3), 591−594.
(84) Yang, Y.; Lepech, M. D.; Yang, E.-H.; Li, V. C. Autogenous Healing of Engineered Cementitious Composites under Wet−Dry Cycles. *Cem. Concr. Res.* **2009**, *39* (5), 382−390.
(85) Yang, T.; Keller, B.; Magyari, E.; Hametner, K.; Günther, D. Direct Observation of the Carbonation Process on the Surface of Calcium Hydroxide Crystals in Hardened Cement Paste Using an Atomic Force Microscope. *J. Mater. Sci.* **2003**, *38*, 1909−1916.
(86) García-González, C. A.; Hidalgo, A.; Andrade, C.; Alonso, M. C.; Fraile, J.; López-Periago, A. M.; Domingo, C. Modification of Composition and Microstructure of Portland Cement Pastes as a Result of Natural and Supercritical Carbonation Procedures. *Ind. Eng. Chem. Res.* **2006**, *45* (14), 4985−4992.
(87) Neville, A. M. *Properties of Concrete*; Longman London, 1995; Vol. *4*, p 26.
(88) Groves, G. W.; Brough, A.; Richardson, I. G.; Dobson, C. M. Progressive Changes in the Structure of Hardened C3S Cement Pastes Due to Carbonation. *J. Am. Ceram. Soc.* **1991**, *74* (11), 2891−2896.
(89) Thiery, M.; Villain, G.; Dangla, P.; Platret, G. Investigation of the Carbonation Front Shape on Cementitious Materials: Effects of the Chemical Kinetics. *Cem. Concr. Res.* **2007**, *37* (7), 1047−1058.
(90) Cizer, Ö.; Van Balen, K.; Elsen, J.; Van Gemert, D. Real-Time Investigation of Reaction Rate and Mineral Phase Modifications of Lime Carbonation. *Constr. Build. Mater.* **2012**, *35*, 741−751.

(91) Galan, I.; Glasser, F. P.; Baza, D.; Andrade, C. Assessment of the Protective Effect of Carbonation on Portlandite Crystals. *Cem. Concr. Res.* **2015**, *74*, 68−77.
(92) Hidalgo, A.; Domingo, C.; Garcia, C.; Petit, S.; Andrade, C.; Alonso, C. Microstructural Changes Induced in Portland Cement-Based Materials Due to Natural and Supercritical Carbonation. *J. Mater. Sci.* **2008**, *43*, 3101−3111.
(93) Richardson, I. G.; Groves, G. W.; Brough, A. R.; Dobson, C. M. The Carbonation of OPC and OPC/Silica Fume Hardened Cement Pastes in Air under Conditions of Fixed Humidity. *Adv. Cem. Res.* **1993**, *5* (18), 81−86.
(94) Wu, L.; Farzadnia, N.; Shi, C.; Zhang, Z.; Wang, H. Autogenous Shrinkage of High Performance Concrete: A Review. *Constr. Build. Mater.* **2017**, *149* (September), 62−75.
(95) Yu, P.; Kirkpatrick, R. J.; Poe, B.; McMillan, P. F.; Cong, X. Structure of Calcium Silicate Hydrate (C-S-H): Near-, Mid-, and Far-infrared Spectroscopy. *J. Am. Ceram. Soc.* **1999**, *82* (3), 742−748.
(96) Yılmaz, B.; Olgun, A. Studies on Cement and Mortar Containing Low-Calcium Fly Ash, Limestone, and Dolomitic Limestone. *Cem. Concr. Compos.* **2008**, *30* (3), 194−201.
(97) Kamali, M.; Ghahremaninezhad, A. Effect of Biomolecules on the Nanostructure and Nanomechanical Property of Calcium-Silicate-Hydrate. *Sci. Rep.* **2018**, *8* (September 2017), No. 9491.
(98) Kamali, M.; Ghahremaninezhad, A. A Study of Calcium-Silicate-Hydrate/Polymer Nanocomposites Fabricated Using the Layer-by-Layer Method. *Materials* **2018**, *11*, 527.
(99) Vladu, C. M.; Hall, C.; Maitland, G. C. Flow Properties of Freshly Prepared Ettringite Suspensions in Water at 25° C. *J. Colloid Interface Sci.* **2006**, *294* (2), 466−472.
(100) Kißling, P. A.; Lübkemann, F.; von Bronk, T.; Cotardo, D.; Lei, L.; Feldhoff, A.; Lohaus, L.; Haist, M.; Bigall, N. C. Influence of Low-Pressure Treatment on the Morphological and Compositional Stability of Microscopic Ettringite. *Materials* **2021**, *14* (11). 2720.
(101) Taylor, H. F. W. *Cement Chemistry*; Thomas Telford London, 1997; Vol. *2*, p 113.
(102) Dent Glasser, L.; Lachowski, E. E.; Mohan, K.; Taylor, H. F. W. A Multi-Method Study of C3S Hydration. *Cem. Concr. Res.* **1978**, *8* (6), 733−739.
(103) Mills, R.; Lobo, V. M. M. *Self-Diffusion in Electrolyte Solutions: A Critical Examination of Data Compiled from the Literature*; Elsevier, 1989; p 40.
(104) Snoeck, D. Self-Healing and Microstructure of Cementitious Materials with Microfibres and Superabsorbent Polymers, Doctoral dissertation, Ghent University, 2016.
(105) Yang, E.-H. Designing Added Functions in Engineered Cementitious Composites. 2008.
(106) Mignon, A.; Vermeulen, J.; Snoeck, D.; Dubruel, P.; Van Vlierberghe, S.; De Belie, N. Mechanical and Self-Healing Properties of Cementitious Materials with PH-Responsive Semi-Synthetic Superabsorbent Polymers. *Mater. Struct.* **2017**, *50* (6), No. 238, DOI: 10.1617/s11527-017-1109-4.

https://doi.org/10.1021/acssuschemeng.4c02045
ACS Sustainable Chem. Eng. 2024, 12, 8261−8275